nature astronomy

Supplementary information https://doi.org/10.1038/s41550-026-02953-z

An eccentric massive protobinary assembled via a core-merger parabolic encounter

In the format provided by the authors and unedited

Supplementary Information

Supplementary Discussion 1. Reliability of continuum image fitting and astrometry measurement

The deconvolved source morphologies from continuum image fitting are generally consistent from 3 to 0.6 mm (Extended Data Fig. 4). However, the deconvolved ellipses at 7 and 13 mm deviate from those measured at higher frequencies, likely owing to the larger beam sizes and increased source blending, particularly at 13 mm. In addition, the free–free continuum becomes increasingly optically thick toward lower frequencies, enlarging the optically thick region and causing departures from the Gaussian assumption. The deconvolved morphology at 0.3 mm also differs markedly from that at 3−0.6 mm despite a comparable beam size. This difference is attributed to the increasing contribution of optically thick dust emission at 0.3 mm, which has a spatial distribution distinct from that of the ionized gas traced at longer wavelengths. Consistently, the peak brightness temperatures of Sources A and B at 0.3 mm are 133 K and 88 K, respectively, indicative of optically thick dust emission. Despite these effects, the observed deviations at the higher-frequency bands exhibit largely isotropic residuals and are therefore not expected to introduce significant systematic biases in the measured source positions.

The positional uncertainties from Gaussian image fitting generally scale inversely with the peak signal-to-noise ratio. However, such uncertainties can underestimate the true astrometric errors when systematic effects such as source blending, calibration residuals, and departures from the assumed source morphology are present[1,2]. In the present data, the astrometric accuracy can be affected by source blending, particularly at 1.3 cm, and by intrinsic shifts of the emission peaks arising from wavelength-dependent optical-depth effects. To account for such uncharacterized systematics in the proper-motion analysis, we introduced an isotropic intrinsic-scatter term, $\sigma_{\rm int}$, following the standard approach[3]. The inferred value, $\sigma_{\rm int} = 1.3^{+0.5}_{-0.3}$ mas (Fig. 1e,f), therefore provides an empirical estimate of the residual astrometric uncertainty not captured by the formal image-fitting errors.

To further assess the robustness of the astrometry, we performed visibility-domain fitting in addition to image-domain Gaussian fitting (Supplementary Figs. 2 and 3). The positional offsets between the two methods are approximately 2 mas at 1.3 cm and approximately 0.5 mas at the other wavelengths. These differences are comparable to the inferred intrinsic-scatter term and therefore remain within the adopted astrometric uncertainty budget.

Supplementary Discussion 2. Robustness of the orbital proper-motion measurement

Several effects could potentially mimic or bias the measured relative motion between the two sources. One possibility is wavelength-dependent centroid shifts caused by optical-depth variations. If such effects dominated the measured positions, the relative offsets would be expected to follow the ordering of observing wavelength. Instead, the measured positional offsets of Source B relative to Source A follow the temporal sequence of the observing epochs rather than the wavelength sequence, indicating that the observed shifts are primarily driven by source proper motion.

Another possible origin of the observed position changes is variability associated with radio jets, which has been reported in centimeter observations of forming stars[4–6]. However, the measured relative motion of approximately 10 km s^{-1} is substantially lower than typical jet velocities of 100−1000 km s^{-1}[7]. Moreover, the relative motion remains clearly detectable at millimeter wavelengths, where contamination from free–free jet emission is expected to be minimal. For example, a positional shift is evident between the 1.3-mm observations obtained in 2017 and the 0.3-mm observations obtained in 2024. Furthermore, although the measured proper-motion direction is broadly aligned with the expected jet axis of Source B, no jet is detected toward this source in the free–free continuum (Extended Data Fig. 5).

Taken together, these tests support that the measured relative motion is dominated by binary orbital motion. Residual contributions from jet variability, wavelength-dependent optical-depth effects, and other systematic uncertainties are incorporated into the intrinsic-scatter term adopted in the astrometric analysis.

Supplementary Discussion 3. Evidence for non-LTE effects in the hydrogen recombination lines

The observed hydrogen recombination line (HRL) fluxes exhibit a spectral index significantly steeper than the value of 1 expected for optically thin LTE emission. At low frequencies, such behavior can be partly attributed to increasing free-free continuum optical depth. However, the steep trend persists toward higher frequencies, where optical-depth effects alone cannot account for the observed fluxes. In addition, several high-frequency HRLs display non-Gaussian spectral profiles, most notably the H26α line toward Source A (Extended Data Fig. 3).

These characteristics suggest that the HRL emission is affected by departures from LTE. One possible explanation is maser amplification, which has been predicted and observed for HRLs with principal quantum numbers $n \sim 7$–39[8]. Such non-LTE effects can modify both the line strengths and spectral profiles, potentially contributing to the discrepancies between the observed HRL fluxes and simple LTE expectations. Since our SED and HRL fitting adopts an LTE treatment as a first-order approximation, only the lower-frequency HRL fluxes are fitted (see Method and Fig. 4).

Supplementary Discussion 4. Influence of proper-motion measurements and prior assumptions on orbital constraints

In previous work on this source[9], only radial velocity and single-epoch astrometric data were available to constrain the orbital properties. To assess the impact of the newly measured proper motions, we performed an additional orbital fit (Orbital Fitting 3) using only the same single-epoch 1.3 mm data. Although the overall constraint on eccentricity is weak, as expected (Supplementary Fig. 8), the observed relative proper-motion components ($v_{\mathrm{R.A.}}$ and $v_{\mathrm{Dec.}}$) can be reproduced only by models with high eccentricities (Supplementary Fig. 9). This comparison demonstrates that the multi-epoch astrometric measurements provide a critical new constraint on the orbital architecture of the system.

In Orbital Fitting 1 and 2, even when the total system mass is constrained by independent observations, the eccentricity remains imperfectly determined owing to the limited orbital coverage. A pronounced tail toward lower eccentricities is present in the posterior distributions obtained from Orbital Fitting 1 and 2 (Fig. 5a, Extended Data Fig. 6a). Part of this behavior reflects the adopted prior assumptions. In Orbital Fitting 1, a log-uniform prior on eccentricity places greater weight on low-eccentricity solutions, resulting in a broader posterior distribution extending toward smaller eccentricities. In Orbital Fitting 2, adopting a uniform prior over $0 < e < 2$ produces a posterior that is more sharply peaked and symmetric around $e \approx 1$ (see also Supplementary Fig. 7). Nevertheless, both fitting approaches consistently favor solutions clustered around $e \approx 1$ over the independently inferred mass range of the system. Lower-eccentricity bound orbits remain viable, but near-parabolic solutions are statistically preferred by the current data.

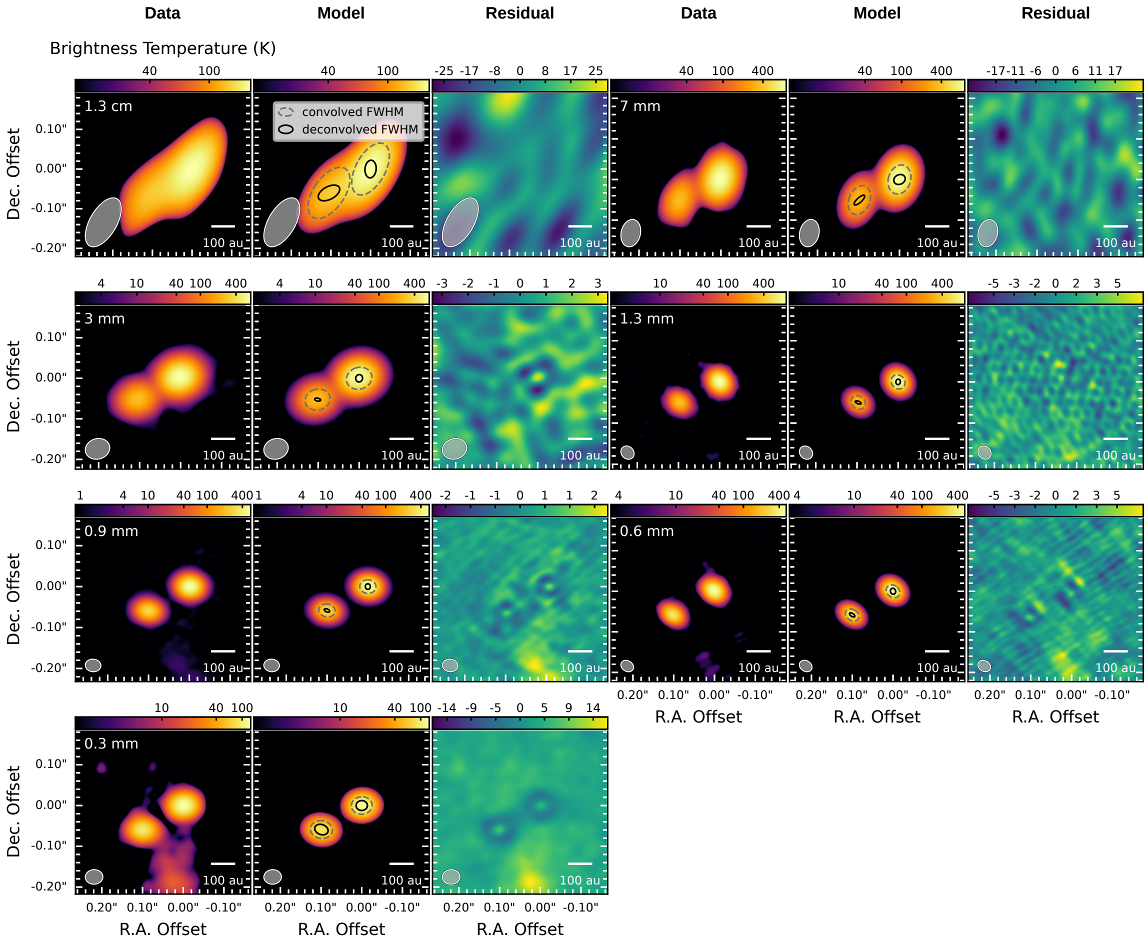

Supplementary Figure 1 | 2D Gaussian fits to the continuum images. In each panel, the convolved and deconvolved Gaussian components are shown as grey dashed and black solid ellipses, respectively. Grey ellipses at lower-left corners show the synthesized beam sizes. Scale bars indicate a physical length of 100 au. Residuals are generally below the 3σ level.

Supplementary Table 1 | 2D Gaussian Fitting to the Continuum Images

Wavelength (mm)	Source	Deconvolved Size (FWHM) (mas×mas)	Deconvolved P.A. (°)	$I_\nu^{\rm peak}$ (K)	S_ν[a] (mJy)	$\Delta\alpha$[b] (mas)	$\Delta\delta$[c] (mas)
13	A	$45\pm16 \times 28\pm11$	175 ± 56	369.7 ± 9.7	1.64 ± 0.13	105.02 ± 3.13	-60.26 ± 4.60
	B	$59\pm26 \times 32\pm15$	118 ± 27	166.7 ± 10.0	0.80 ± 0.12		
7	A	$29\pm2 \times 23\pm2$	116 ± 15	968.5 ± 7.3	5.5 ± 0.3	97.79 ± 0.46	-50.76 ± 0.77
	B	$33\pm5 \times 12\pm6$	132 ± 12	348.6 ± 7.2	1.9 ± 0.1		
3	A	$18.3\pm0.4 \times 16.8\pm0.5$	165 ± 12	710.9 ± 1.0	16.6 ± 0.8	101.23 ± 0.11	-52.63 ± 0.08
	B	$14.9\pm1.4 \times 7.1\pm2.8$	78 ± 10	261.1 ± 1.0	5.8 ± 0.3		
1.3	A	$13.3\pm0.2 \times 10.9\pm0.3$	173 ± 5	965.8 ± 1.6	50.5 ± 2.5	97.10 ± 0.07	-49.97 ± 0.07
	B	$15.0\pm0.6 \times 6.3\pm1.0$	70 ± 4	355.0 ± 1.6	18.1 ± 0.9		
0.9	A	$13.76\pm0.08 \times 12.40\pm0.14$	178 ± 4	560.0 ± 0.5	75 ± 4	100.20 ± 0.04	-58.39 ± 0.03
	B	$14.0\pm0.3 \times 7.3\pm0.3$	68 ± 4	289.1 ± 0.5	37 ± 2		
0.6	A	$15.0\pm0.3 \times 12.6\pm0.4$	17 ± 6	525.4 ± 1.5	105 ± 11	100.20 ± 0.08	-58.32 ± 0.07
	B	$14.8\pm0.4 \times 7.4\pm0.4$	57 ± 2	340.7 ± 1.5	63 ± 6		
0.3	A	$28\pm4 \times 24\pm3$	92 ± 70	133.3 ± 4.4	188 ± 23	99.17 ± 1.42	-58.97 ± 1.04
	B	$34\pm6 \times 25\pm6$	69 ± 45	88.1 ± 4.5	133 ± 28		

Notes. (a) Uncertainties include contributions from CASA *imfit*, flux calibration, and variations between different configurations or LSB/USB images. (b) Relative R.A. offset of Source B with respect to Source A. (c) Relative Dec. offset of Source B with respect to Source A.

Supplementary Table 2 | Properties of HRL emissions

HRL	Frequency (GHz)	Source	Channel Width (km s^{-1})	Channel Noise (mJy $beam^{-1}$, K)	I_ν^{peak} (K)	V_{center} (km s^{-1})	FWHM (km s^{-1})	Total Flux[a] (Jy km s^{-1})
H42α	85.688	A	5	0.6, 33	263 ± 26	12.4 ± 1.2	39.2 ± 2.9	0.22 ± 0.01
		B	5	0.6, 33	—	—	—	0.091 ± 0.005
H40α	99.023	A	5	0.5, 29	401 ± 25	13.7 ± 0.8	40.4 ± 2.9	0.37 ± 0.02
		B	5	0.5, 29	—	—	—	0.109 ± 0.005
H30α	231.901	A	1	1.8, 38	1965 ± 19	14.8 ± 0.1	39.5 ± 0.3	5.0 ± 0.3
		B	5	0.8, 17	155 ± 13	25.0 ± 1.5	54.2 ± 3.5	0.95 ± 0.05
H26α	353.623	A	1	0.9, 9	2697 ± 49	14.7 ± 0.3	43.0 ± 0.6	13.7 ± 0.7
		B	1	0.9, 9	318 ± 5	24.6 ± 0.2	49.9 ± 0.6	2.0 ± 0.1
H19α	888.047	A	1	45.3, 40	951 ± 15	17.6 ± 0.2	44.7 ± 0.5	55.8 ± 2.8
		B	5	22.8, 20	213 ± 15	18.8 ± 1.3	55.8 ± 3.0	19.4 ± 1.0

Notes. (a) HRL total flux uncertainties combine the flux calibration error and the photometric error from the moment 0 maps.

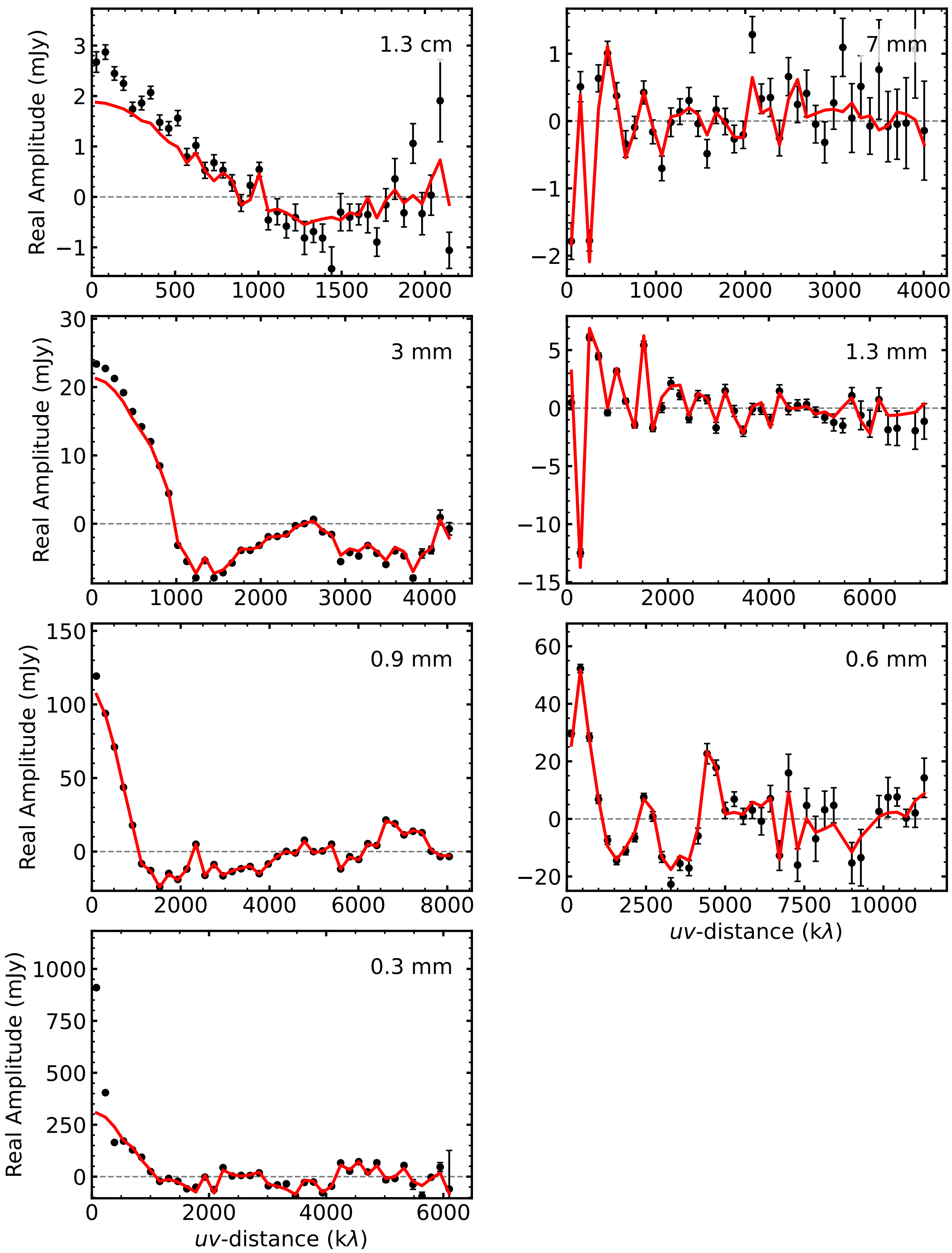

Supplementary Figure 2 | Two-component Gaussian fits to the continuum visibility data. Black points show the real part of the visibilities, binned into 40 points for clarity. Error bars denote the standard error of the mean real visibility in each bin. The grey dashed horizontal line marks zero real visibility. Red curves show the corresponding best-fitting models.

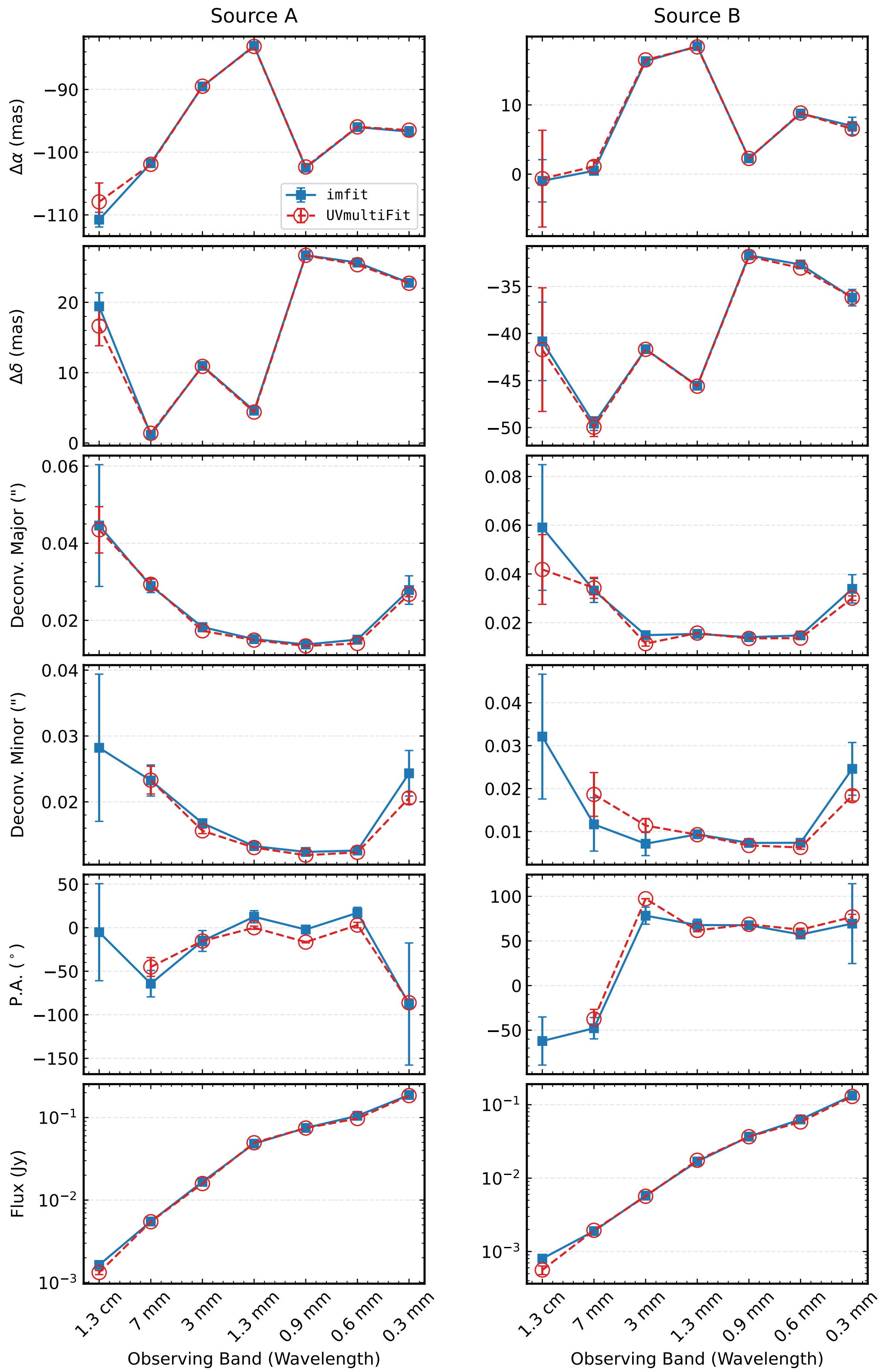

Supplementary Figure 3 | Comparison of continuum parameters derived from visibility fitting and image fitting. Results from visibility fitting via *UVmultiFit* are shown with open red circles while those from image fitting via *imfit* are shown with filled blue squares. Error bars indicate uncertainties either derived directly from the fits or propagated from the fitted parameters for the two approaches. Shown parameters include absolute source positions, Gaussian properties, and total flux densities of the two sources. Source positions are expressed as offsets relative to $(\alpha_{\rm ICRS}, \delta_{\rm ICRS}) = (07^{\rm h}32^{\rm m}09.79^{\rm s}, -16^\circ 58' 12''.15)$. In the K band, the Gaussian aspect ratio was fixed during visibility fitting; consequently, the minor-axis FWHM and position angle are not reported for this band.

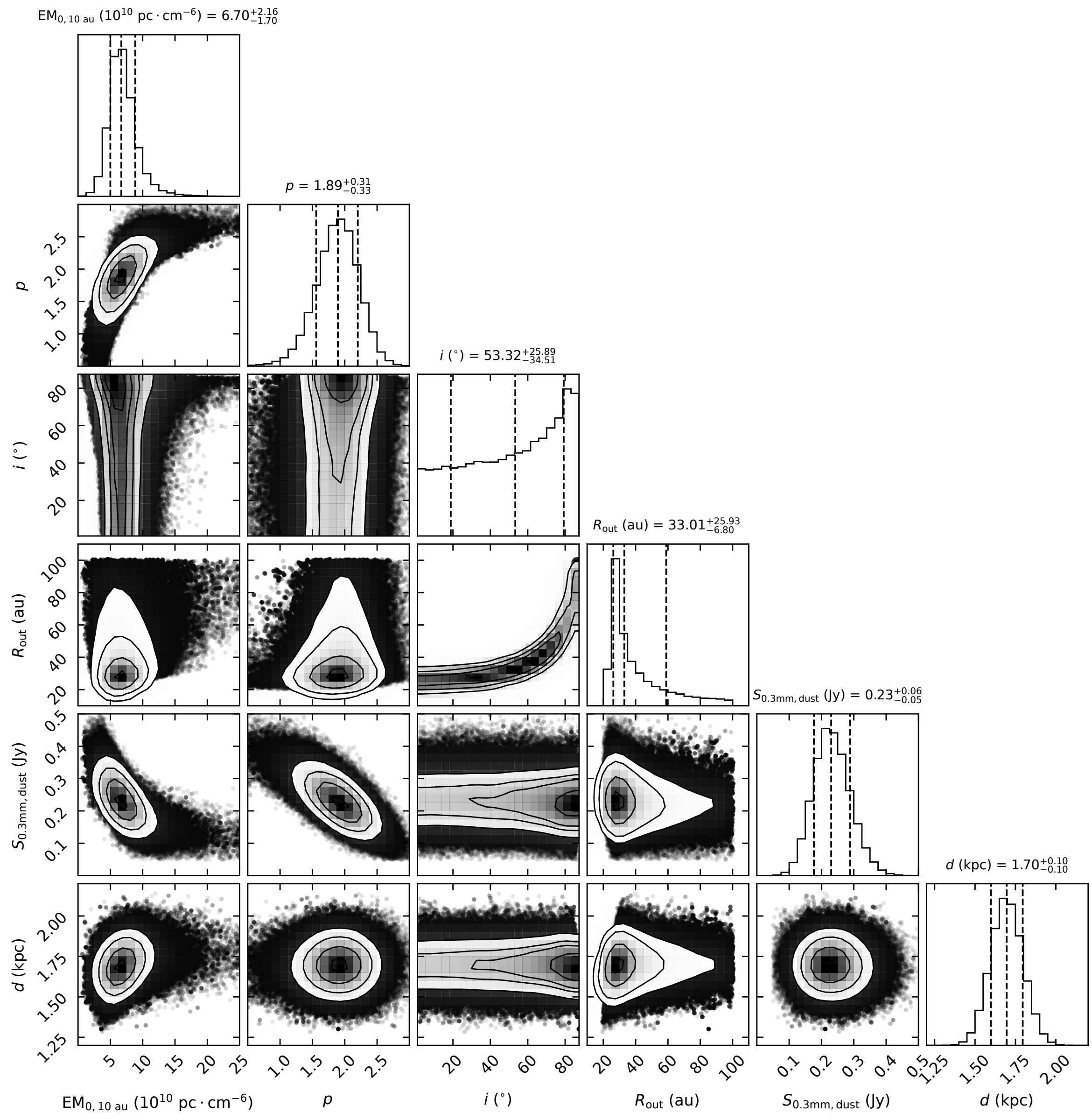

Supplementary Figure 4 | Posterior distributions from the joint fit to continuum SED and HRL fluxes for Source A. The corner plot illustrates the distributions and covariances of the six free parameters in the physical model: the emission-measure normalization, EM_0, at the reference radius $r_0 = 10$ au; the power-law index of the emission-measure distribution, p; the outer truncation radius of the ionized disk, r_{out}; the disk inclination, i; the dust-continuum normalization at 0.3 mm, $S_{0.3,mm,dust}$; and the distance to the system, d. The source distance is treated as a free parameter to account for its uncertainty. In the marginal distributions, the dashed lines indicate the 16th, 50th (median), and 84th percentiles.

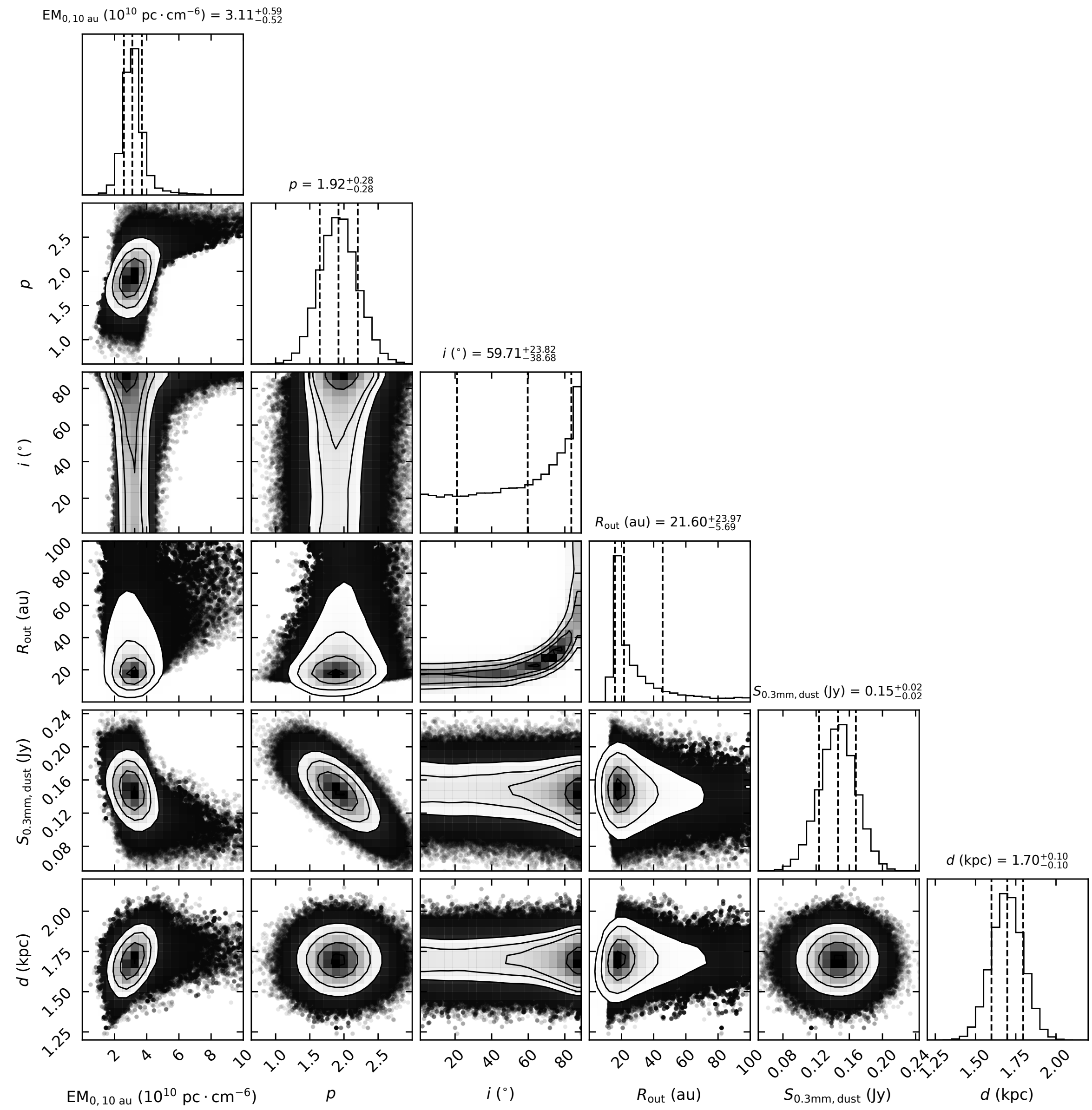

Supplementary Figure 5 | Posterior distributions from the joint fit to continuum SED and HRL fluxes for Source B. The corner plot illustrates the distributions and covariances of the six free parameters in the physical model: the emission-measure normalization, EM_0, at the reference radius $r_0 = 10$ au; the power-law index of the emission-measure distribution, p; the outer truncation radius of the ionized disk, r_{out}; the disk inclination, i; the dust-continuum normalization at 0.3 mm, $S_{0.3,\mathrm{mm,dust}}$; and the distance to the system, d. The source distance is treated as a free parameter to account for its uncertainty. In the marginal distributions, the dashed lines indicate the 16th, 50th (median), and 84th percentiles.

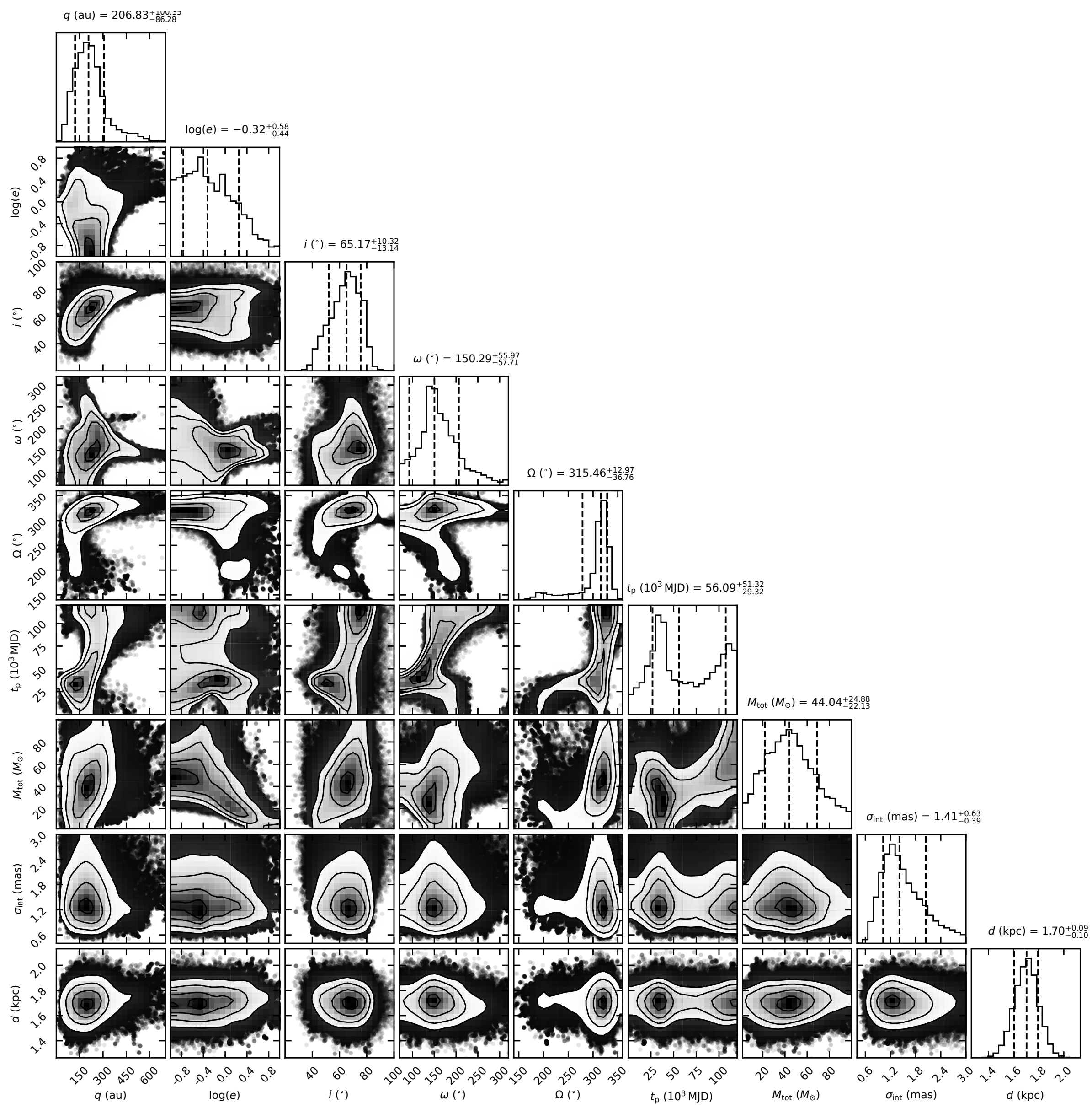

Supplementary Figure 6 | Posterior samples from the unified orbital fitting (Orbital Fitting 1). Nine free parameters for the fitting are shown: periapsis distance q, eccentricity e, inclination i, argument of periapsis ω, longitude of ascending node Ω, time of periapsis $t_{\rm p}$, and total mass $M_{\rm tot}$, intrinsic scatter $\sigma_{\rm int}$, and distance to this system d. The source distance is treated as a free parameter to account for its uncertainty. In the marginal distributions, the dashed lines indicate the 16th, 50th (median), and 84th percentiles.

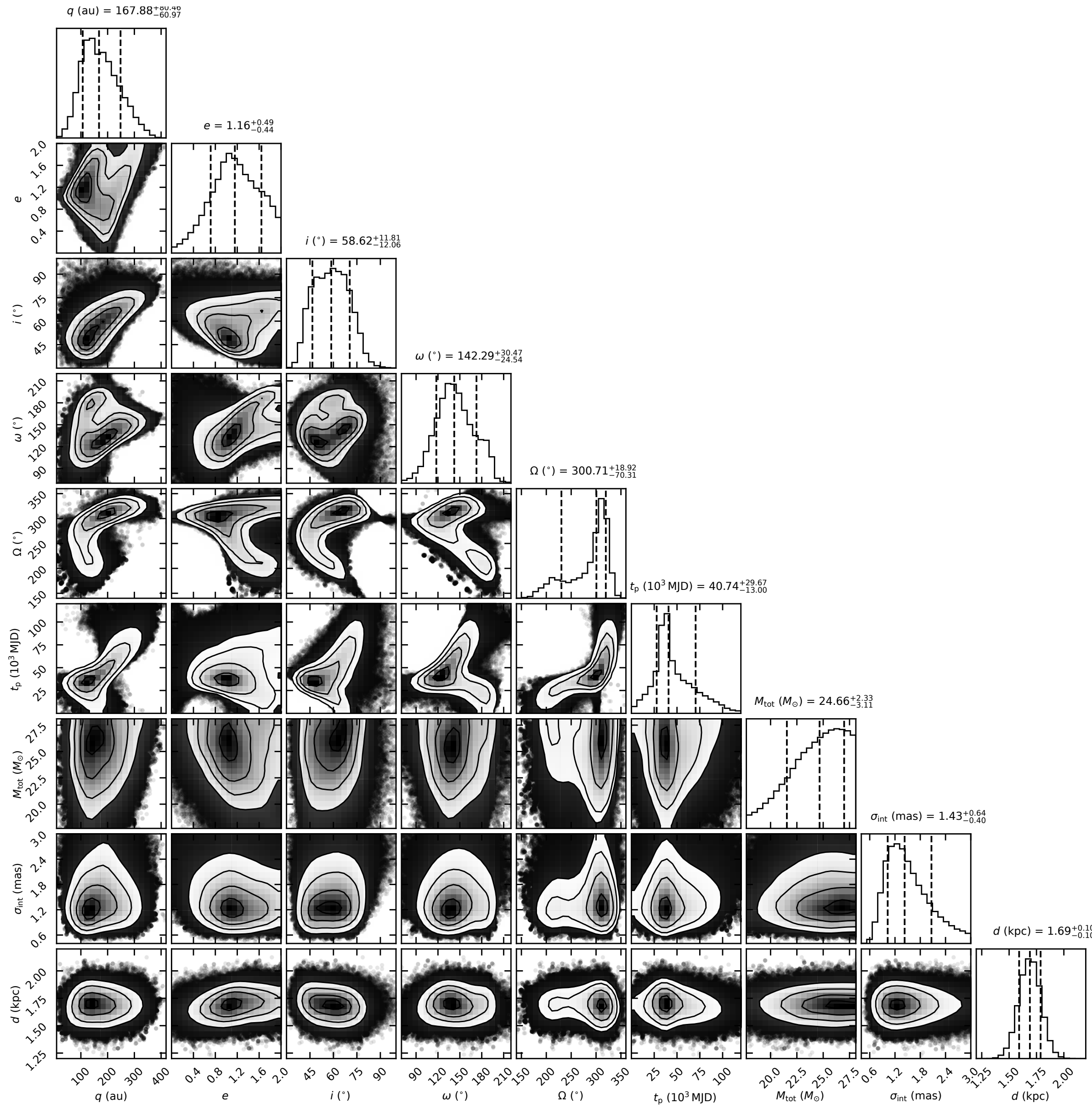

Supplementary Figure 7 | Posterior samples from the unified orbital fitting with a constrained mass range (Orbital Fitting 2). A truncated Gaussian prior for M_{tot} is adopted, with mean 25.9 $M_{\odot}$, standard deviation 4.0 $M_{\odot}$, and hard bounds of 17.7–28.1 $M_{\odot}$. The eccentricity prior is set to be uniform between $0-2$. Nine free parameters are shown: periapsis distance q, eccentricity e, inclination i, argument of periapsis ω, longitude of ascending node Ω, time of periapsis t_{p}, and total mass M_{tot}, intrinsic scatter σ_{int}, and distance to this system d. The source distance is treated as a free parameter to account for its uncertainty. In the marginal distributions, the dashed lines indicate the 16th, 50th (median), and 84th percentiles. The fitting has a weighted reduced chi-square of $\chi^2_{\text{reduced}} = 1.57^{+0.74}_{-0.54}$ over the full posterior.

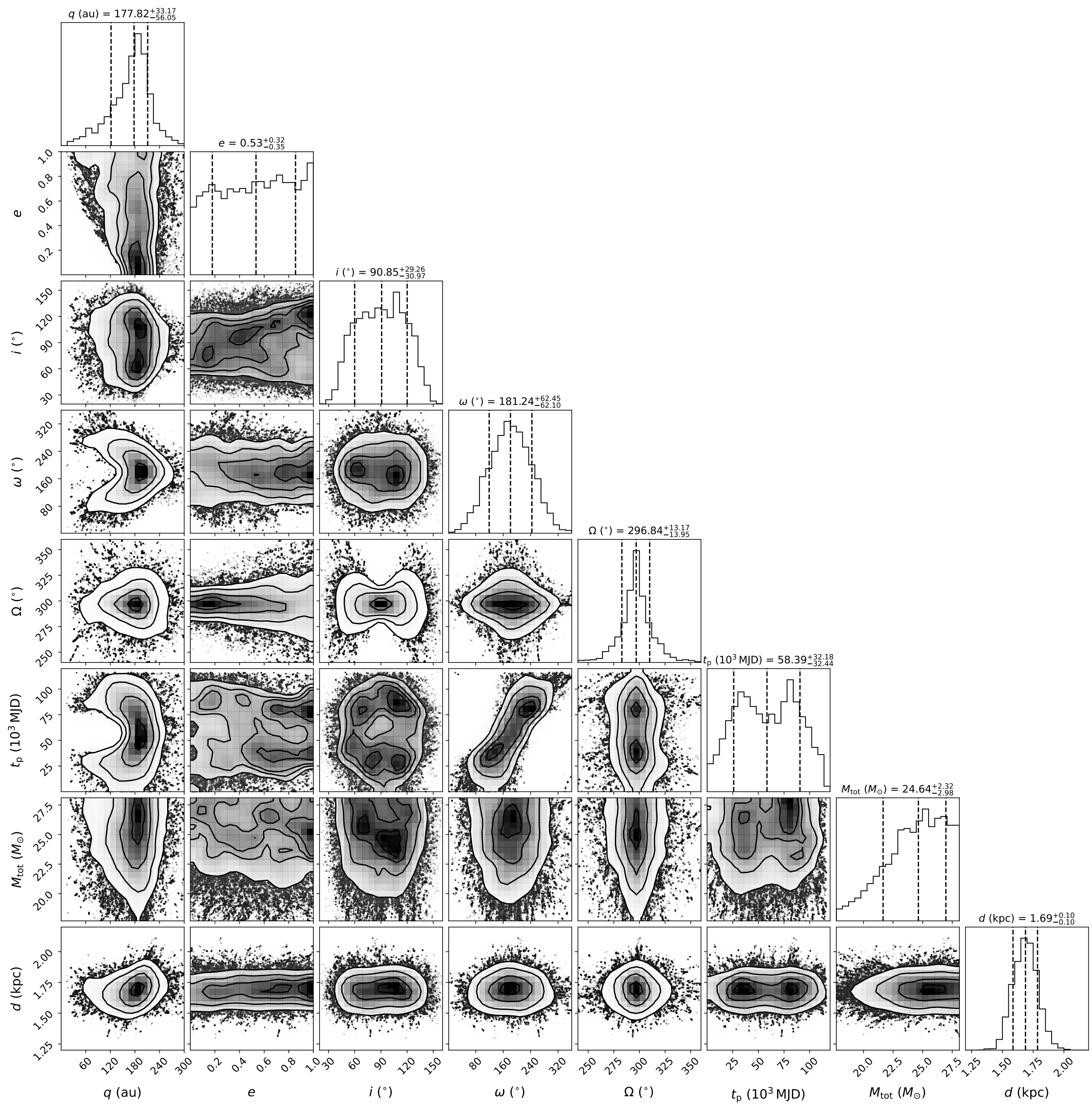

Supplementary Figure 8 | Posterior samples from the elliptical orbital fitting to the 1.3 mm data alone (Orbital Fitting 3). The prior of eccentricity is set to uniform between $0-1$ and a truncated Gaussian prior is adopted for M_{tot}, with mean 25.9 $M_{\odot}$, standard deviation 4.0 $M_{\odot}$, and hard bounds of 17.7–28.1 $M_{\odot}$. Eight free parameters are shown: periapsis distance q, eccentricity e, inclination i, argument of periapsis ω, longitude of ascending node Ω, time of periapsis t_{p}, and total mass M_{tot} and distance to this system d. The source distance is treated as a free parameter to account for its uncertainty. In the marginal distributions, the dashed lines indicate the 16th, 50th (median), and 84th percentiles.

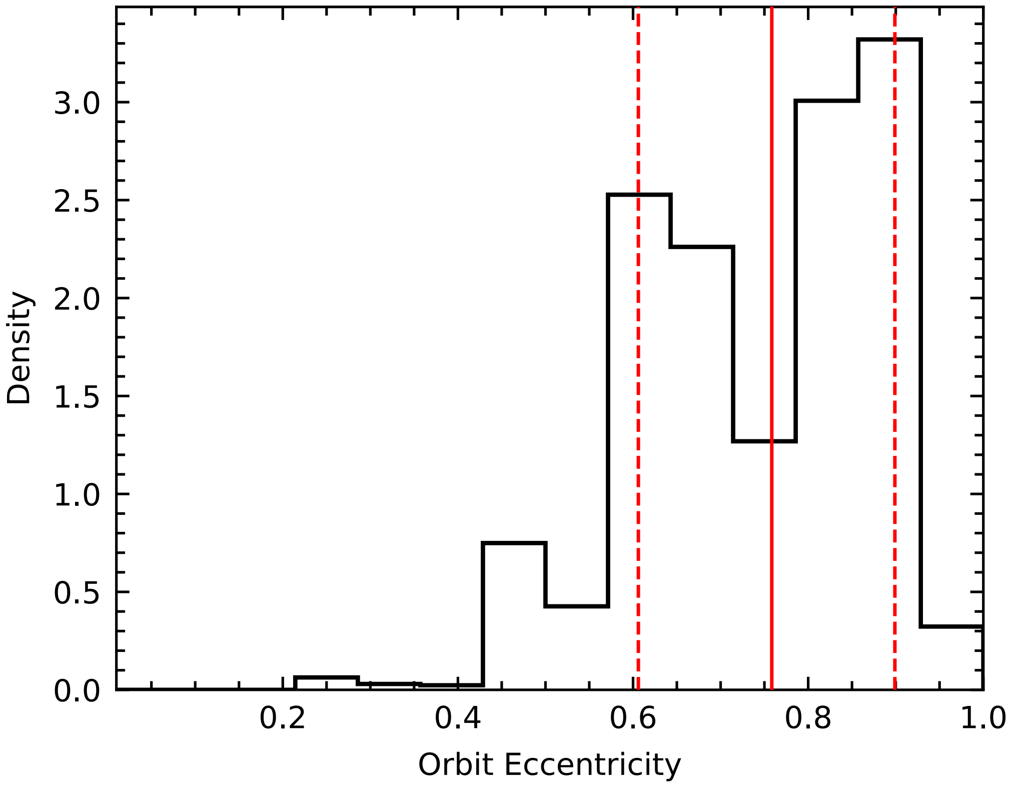

Supplementary Figure 9 | Eccentricity constraints from single-epoch orbital fitting (Orbital Fitting 3). The eccentricity distribution is derived from the orbit solutions in Fitting 3 that be able to reproduce the observed $v_{\mathrm{R.A.}}$ and $v_{\mathrm{Dec.}}$. The 16th, 50th (median), and 84th percentiles are indicated with vertical red lines.

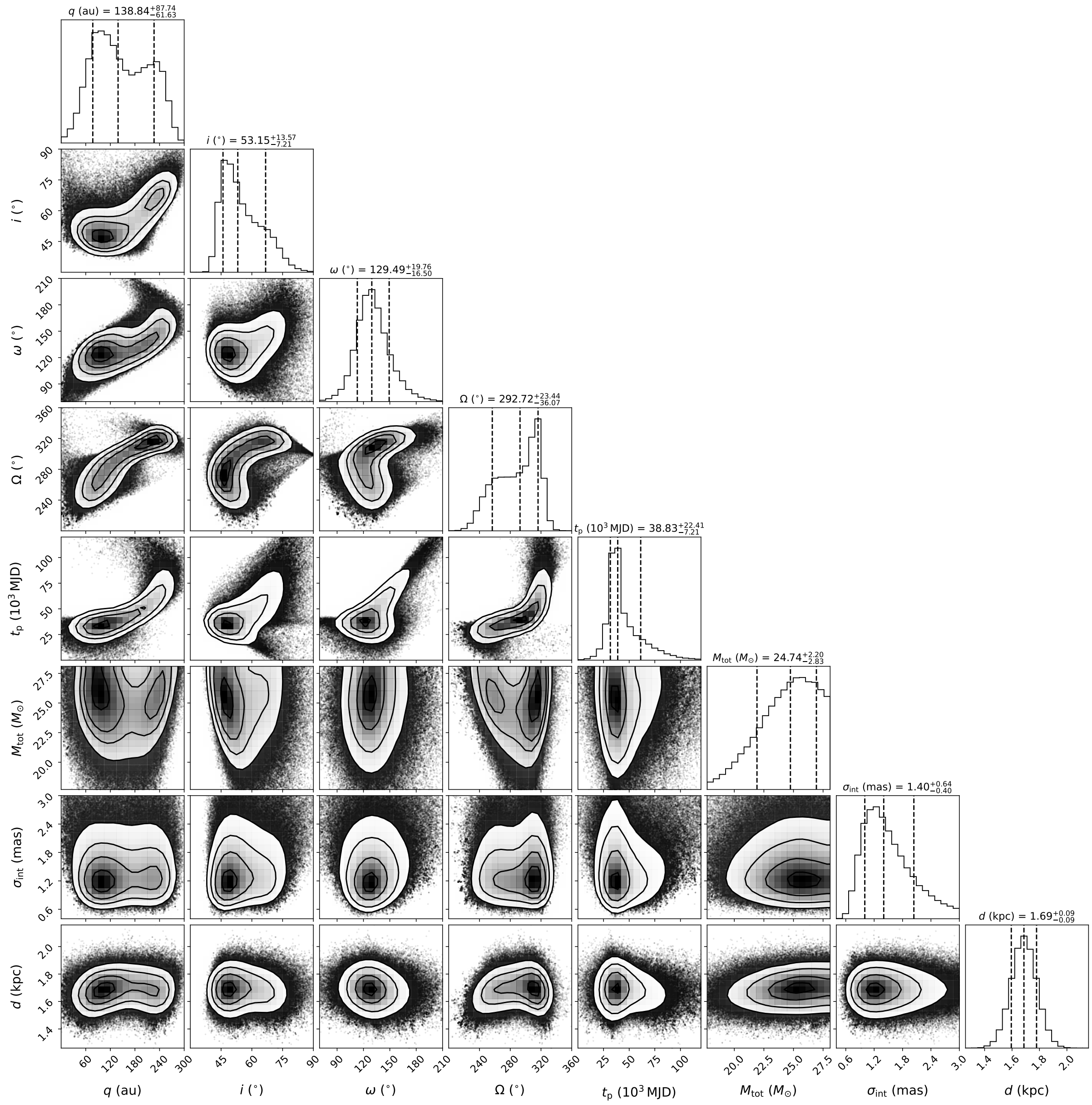

Supplementary Figure 10 | Posterior samples from the fiducial parabolic orbital fitting with constrained mass range (Orbital Fitting 4). A truncated Gaussian prior for $M_{\rm tot}$ is adopted, with mean 25.9 $M_\odot$, standard deviation 4.0 $M_\odot$, and hard bounds of 17.7–28.1 $M_\odot$. Eight free parameters are shown: periapsis distance q, inclination i, argument of periapsis ω, longitude of ascending node Ω, time of periapsis $t_{\rm p}$, and total mass $M_{\rm tot}$, intrinsic scatter $\sigma_{\rm int}$, and distance to this system d. The source distance is treated as a free parameter to account for its uncertainty. In the marginal distributions, the dashed lines indicate the 16th, 50th (median), and 84th percentiles. The fitting has a weighted reduced chi-square of $\chi^2_{\rm reduced} = 1.35^{+0.65}_{-0.46}$ over the full posterior.

References

[1] Condon, J. J. Errors in Elliptical Gaussian Fits. *Publ. Astron. Soc. Pac.* **109**, 166–172 (1997).

[2] Hernández Garnica, R. *et al.* Accurate proper motions of the protostellar binary system L 1551 IRS 5. *Mon. Not. R. Astron. Soc.* **535**, 2948–2969 (2024).

[3] Hogg, D. W., Bovy, J. & Lang, D. Data analysis recipes: Fitting a model to data. *arXiv e-prints* arXiv:1008.4686 (2010).

[4] Zapata, L. A. *et al.* ALMA reveals a candidate hot and compact disc around the O-type protostar IRAS 16547-4247. *Mon. Not. R. Astron. Soc.* **447**, 1826–1833 (2015).

[5] Cesaroni, R. *et al.* Radio outburst from a massive (proto)star. II. A portrait in space and time of the expanding radio jet from S255IR NIRS 3. *Astron. Astrophys.* **680**, A110 (2023).

[6] Cesaroni, R. *et al.* Radio outburst from a massive (proto)star. III. Unveiling the bipolarity of the radio jet from S255IR NIRS 3. *Astron. Astrophys.* **683**, L15 (2024).

[7] Anglada, G., Rodríguez, L. F. & Carrasco-González, C. Radio jets from young stellar objects. *Astron. Astrophys. Rev.* **26**, 3 (2018).

[8] Zhang, Q., Claus, B., Watson, L. & Moran, J. Angular Momentum in Disk Wind Revealed in the Young Star MWC 349A. *Astrophys. J.* **837**, 53 (2017).

[9] Zhang, Y. *et al.* Dynamics of a massive binary at birth. *Nat. Astron.* **3**, 517–523 (2019).